The SπRIT experiment: Studying the density dependence of the symmetry energy via heavy RI collisions

T. Isobe,[*1] M. Kurata-Nishimura,[*1] W. G. Lynch,[*2] and M. B. Tsang[*2] for the SπRIT Collaboration

The nuclear Equation of State (EoS) is a fundamental property of nuclear matter that describes the relationships between the parameters for a nuclear system, such as energy, density and temperature. An international collaboration named SπRIT was formed in 2009 to study the density dependence of the symmetry energy term in the nuclear EoS. One of the main devices in experimental setup is a Time Projection Chamber (TPC) which was installed into the SAMURAI dipole magnet. The TPC measures charged pions, protons and light ions simultaneously in heavy ion collisions. An experiment with heavy-ion collisions of a neutron-rich Sn isotope and a neutron-deficient Sn isotope at E_{lab} = 270 MeV/nucleon was performed in 2016. Simultaneous measurement of neutron is possible with neutron detectors at SAMURAI. Those measurements are used as probes to study the EoS of asymmetric dense nuclear matter, which is essential to understand the properties of neutron stars.

Introduction

A neutron star (NS) is believed to be created as a remnant of a supernova explosion. The properties of a neutron star can be described with the thermodynamical character (Equation of State, EoS) of nuclear matter which gives the basic relationships between the energy (E), which is expressed as pressure (P), temperature (T), density (ρ), and isospin asymmetry ($\delta = |\rho_n - \rho_p|/\rho$):

$$E(T,\rho,\delta) = E(T,\rho,\delta=0) + E_{\rm sym}(T,\rho)\delta^2 + O \quad (1)$$

where, it can be decomposed into a symmetric matter contribution that is independent of the isospin asymmetry and a symmetry energy term, $E_{\rm sym}$, proportional to the square of the asymmetry.[1,2] This second term describes the dependence of the EoS on asymmetry.

Experimental information about the EoS is important to understand neutron star observables such as stellar radii, moments of inertia, and crustal vibration frequencies. Important information has been obtained from astronomical observations. For example, the observations of a two solar mass neutron star Pulsar J1614-2230,[3] and Pulsar J0348 + 043[4] place significant constraints on the maximum energy densities, and pressures achieved at the centers of neutron stars. To support such a large stellar mass and to prevent it from collapsing into a black hole, the EoS must have a strong density dependence at high densities.

A quantitative information about the EoS was recently obtained from analyses of the late-stage in spiral dynamics of the GW170817 neutron star merger event.[5] Analysis now provides bounds on the dimensionless deformability of neutron stars of $\Lambda = 190^{+390}_{-120}$ and radii of 11.9 ± 1.4 km by assuming both stars are described by the same EoS, have low spin, and have 1.4 solar-masses.[5]

Constraining the density dependence of the symmetry energy from heavy-ion collisions

Heavy-ion collisions provide the only means to produce nuclear matter at high density of $\rho > \rho_0$ in the laboratory and study its properties.

Measurements of isoscalar collective vibrations, collective flow and kaon production in energetic nucleus-nucleus collisions have constrained the equation of state for symmetric matter, $E(\rho, \delta = 0)$, for densities ranging from saturation density to five times saturation density.[6–8] The extrapolation of the EoS to neutron-rich matter depends on $E_{\rm sym}(\rho)$.

An experimental constraint on the density dependence of the symmetry energy in the vicinity of high density accomplishes several objectives:

- It provides an important constraint on the total pressure supporting a neutron star at density that dominates both the correlation between a neutron star's mass and its radius and the neutron star deformability as observed in neutron star mergers.
- It provides a decomposition of EoS into symmetric matter and symmetry energy contributions. Knowledge of the symmetry energy contributions is essential for understanding the internal structure of a neutron star, the supernovae dynamics, and the importance of cooling via direct and modified URCA processes.

The SπRIT Time Projection Chamber

An international collaboration, SπRIT, was formed by researchers from the USA, Korea, China, Poland, Germany, Japan, and other countries (Fig. 1) to investigate the density dependent symmetry energy by using heavy-ion collision at RIBF.

As the main experimental device for the heavy-ion collision experiments at RIBF, we have constructed a novel detector called the Superconducting Analyzer for MUlti-particles from RAdioIsotope (SAMURAI)

*1 RIKEN Nishina Center
*2 Facility for Rare Isotope Beams, Michigan State University

DOI:10.34448/RIKEN.APR.58-901

Fig. 1. SπRIT Collaboration.

Pion-Reconstruction and Ion-Tracker Time Projection Chamber (SπRIT TPC).[9] Many aspects of the design of the SπRIT TPC resemble those of the EOS TPC, as both detectors measured heavy-ion collisions in a fixed target mode within a dipole magnet of similar design. The SπRIT TPC operates within the SAMURAI dipole, which has a magnet diameter similar to that of the HISS dipole that housed the EOS TPC, but the SAMURAI dipole has a smaller usable gap of 75 cm. Table 1 lists some of the SπRIT TPC operating parameters. An exploded view of the SπRIT TPC is shown in Fig. 2, with key components labeled. The top plate provides the rigid mounting surface for the readout electronics, pad plane, wire planes including gating grid wire,[10] target mechanism, and field cage. Unlike the EOS TPC, we position the wire planes at the top of the field cage, which is attached to the top plate. This configuration protects the pad plane and wire planes from falling objects and facilitates the convective removal of the heat generated by the TPC readout electronics located on top of the TPC. The voltage step-down, which safely interfaces the high voltage of the cathode to ground, is located at the bottom of the enclosure. This structure makes it possible to use gases with lower drift velocities. The experimental campaigns used metallic Sn target foils located 8.6 mm upstream of the entrance window of the field cage using P10 (Ar (90%)—CH_4 (10%)) of 1 atm as the counter gas.

To read out the 12,096 channels of SπRIT TPC,

Table 1. Properties of the SπRIT TPC.

Pad plane area	134.4×86.4 cm^2
Number of pads	12096 (112×108)
Pad size	1.2×0.8 cm^2
Drift length	50.5 cm
Readout sampling frequency	40 MHz
Signal shaping time	117 nsec
Electronic noise	800 q_e
Electric field	125 V/cm
Magnetic field	0.5 T
Drift velocity	5.5 cm/μs

Generic Electronics for TPC (GET),[12] is employed.[13] Figure 3 shows the overview of the GET system for the SπRIT TPC. The AsAd (ASIC and ADC) board is the front-end board for the amplification, shaping and digitization of an analog signal. Each AsAd board contains 4 AGET ASIC chips, FPGA and 4 channel ADC and is connected to the TPC pads via an interface board. The AGET is the ASIC chip specially developed for the GET system.[12] The dynamic range (120 fC to 10 pC), charge polarity (positive or negative), signal peaking time (50 ns to 1 μs) and sampling rate (1 to 100 MHz) are configurable through slow control. Each AGET chip can read out 64 channels. However, for the SπRIT TPC, 63 channels are connected to $7 \times 9 = 63$ TPC pads. The unconnected channel serves as a fixed pattern noise (FPN) line which is used for the evaluation of baseline noise and crosstalk signal through

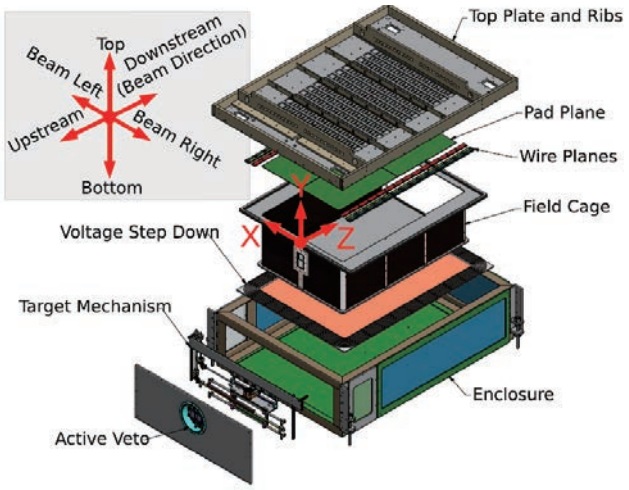

Fig. 2. Exploded view of the SπRIT TPC. Taken from Ref. 11).

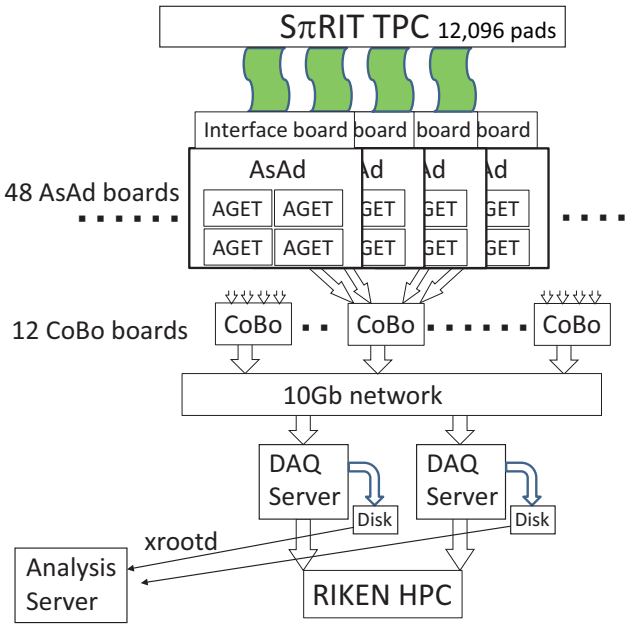

Fig. 3. An overview of the readout system for SπRIT-TPC. 48 AsAd boards are mounted on the TPC. 12 CoBo boards are located outside the SAMURAI magnet. Each CoBo board is connected to 4 AsAd boards. The data buffered in CoBo are continuously sent to data acquisition servers. The data are copied to RIKEN high performance computing clusters. Taken from Ref. 13).

the cables and interface board. For each channel of the AGET chip, a 512 switched capacitor array is integrated as analog memories. The charge stored in the analog memories is converted to digital data when a trigger is made. Each AsAd board is connected to $9 \times 28 = 252$ readout pads out of 108×112 total readout pads. In total, 48 AsAd boards with 192 AGET chips are mounted on top of SπRIT TPC, directly above the pad plane. The configuration of 25 MHz sampling rate, 120 fC dynamic range and shaping time of 117 ns was employed for the SπRIT TPC during the experiments so far. Digitized data in AsAd board are sent to the CoBo (Concentration Board) board which has DDRAM for event buffering. The functionality of the CoBo board includes receiving the trigger, and controlling the AsAd. The data buffered in the CoBo-DDRAM are sent to a DAQ computing cluster.

The detector system of SπRIT TPC allows for an excellent reconstruction of particles and provides isotopic resolution for pions and other light charged particles across a wide range of energy losses and momenta.[14–16)]

Series of heavy ion collision experiment using the SπRIT TPC at RIBF

After the successful commissioning of the SπRIT TPC in 2015,[17)] we carried out two major experimental campaigns in 2016 and 2024. As summarized in Table 2, the first campaign involved Sn + Sn collisions, using radioactive neutron rich projectiles at E = 270 AMeV. The second one was conducted with Xe + Sn collisions, where a primary stable beam at the higher energy of E $\sim$ 320 AMeV was utilized. Figure 4 shows an example of heavy-ion collision event display, negative charged particle which is expected to be negative pion can be seen as well as large number of charged particles. Both experiments were successfully completed, yielding approximately 10 million central collision events for each system. Central collision events were triggered by scintillation counters surrounding SπRIT TPC.[18,19)] As shown in Fig. 5, clean particle ID with isotope resolution from pions through Z = 3 was achieved.

Experimental probes using the SπRIT TPC

In the series of heavy-ion collision experiments, the investigation of π^+ and π^- production and its dependence on the N-Z asymmetry of the colliding system and on the system size was conducted.[20,21)] In addition to pions, the TPC also detected and identified light charged particles such as protons, deuterons, tritons and He isotopes.[22,23)] Coupling the TPC with a neutron detector enabled measurements of neutron-proton spectral single and double ratios. The measurements of pion production,[20,21)] and neutron vs. proton emission and flow[24)] provided significant constraints on the three central properties that are controlled by the effective interactions that must be constrained to address the EoS of asymmetric matter. These include: 1) the density dependence of symmetry energy, 2) the Δ mean field potential, and 3) neutron-proton effective mass splitting at supra-saturation density.

Table 2. Summary of HIC experiments by using the SπRIT TPC.

Primary beam	reaction system	bombarding beam energy	system N/Z
^{238}U	^{132}Sn + ^{124}Sn	270 AMeV	1.56
^{238}U	^{124}Sn + ^{112}Sn	270 AMeV	1.36
^{124}Xe	^{112}Sn + ^{124}Sn	270 AMeV	1.36
^{124}Xe	^{108}Sn + ^{112}Sn	270 AMeV	1.2
	^{136}Xe + ^{124}Sn	320 AMeV	1.44
	^{124}Xe + ^{112}Sn	320 AMeV	1.22

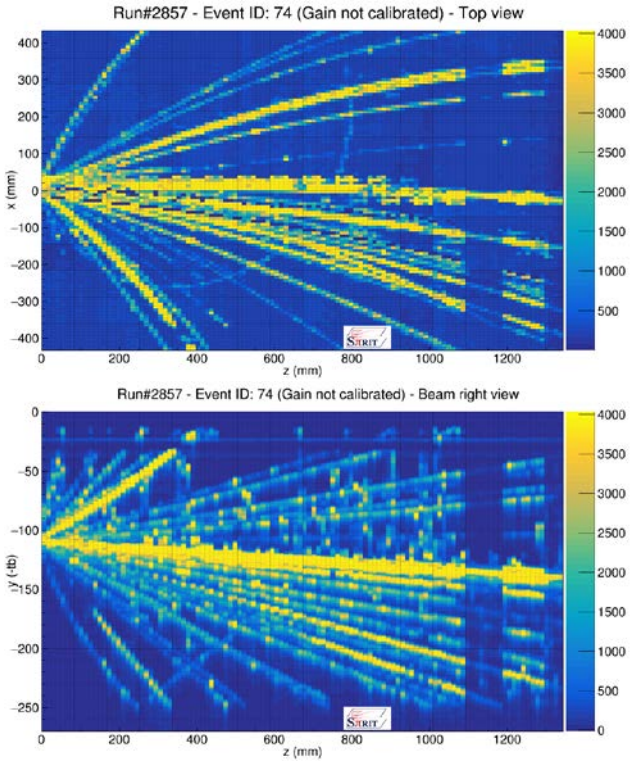

Fig. 4. Event display of a Sn + Sn heavy-ion collision recorded during the 2016 experiments. Top figure and bottom figure show top-view and side-view of the same event, respectively. Sn target is located at $x = 0$ [mm], $y = -117$ [tb]. While many charged particles including heavy fragments from collision move forward, the trajectory of a negative pion can be identified.

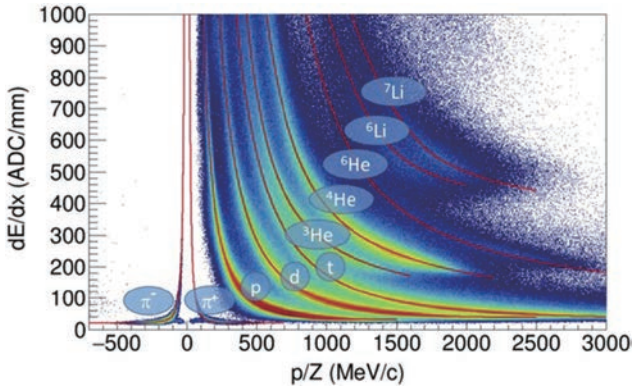

Fig. 5. PID plot for combined ^{132}Sn + ^{124}Sn (top) and ^{108}Sn + ^{124}Sn systems. Expected PID lines are drawn up to lithium isotopes. Taken from Ref. 11).

Pion production

Investigations of pion production in nucleus-nucleus collisions provide unique opportunities to establish meaningful constraints on the density dependence of the symmetry energy at supra-saturation densities. Calculations predict that the relative concentrations of neutrons and protons in the dense interior of a central nucleus-nucleus collision reflect the pressure of the symmetry energy, which is greater for a "stiffer" symmetry energy term with stronger density dependence.[25,26] Since pions are largely produced in the high-density overlap region by Δ resonance production and decay, softer symmetry energies correlate with higher fraction of neutrons in the central density region and, in some transport theories, larger predicted π^-/π^+ yield ratios.

The transverse momentum spectra and multiplicities of negatively and positively charged pions have been measured with high accuracy for central Sn isotope heavy-ion collisions summarized in Table 2.[20,21] Figure 6 shows the single pion spectral ratios for ^{132}Sn + ^{124}Sn (top) and ^{108}Sn + ^{124}Sn reactions. According to the comparison of ratio for high transverse momentum region with one of the transport model numerical calculations, the slope of the symmetry energy, which is called L parameter, is deduced to be $42 \leq$ L ≤ 117 MeV.

Collective flow

Collective flow is a promising observable to constrain nuclear EoS because of its correlation with nuclear pressure. When the mean field is highly repulsive, participant nucleons experience higher pressures which leads to early emission. However, this emission is partially blocked by the spectator nucleons if they have not already moved past the participant region before it can expand into the spectator matter.[6,27,28] The blocking of the expanding participant matter by the spectator nucleons results in azimuthal anisotropies in fragment emissions. In very central collisions, there is very little spectator matter. Thus, emitted particles

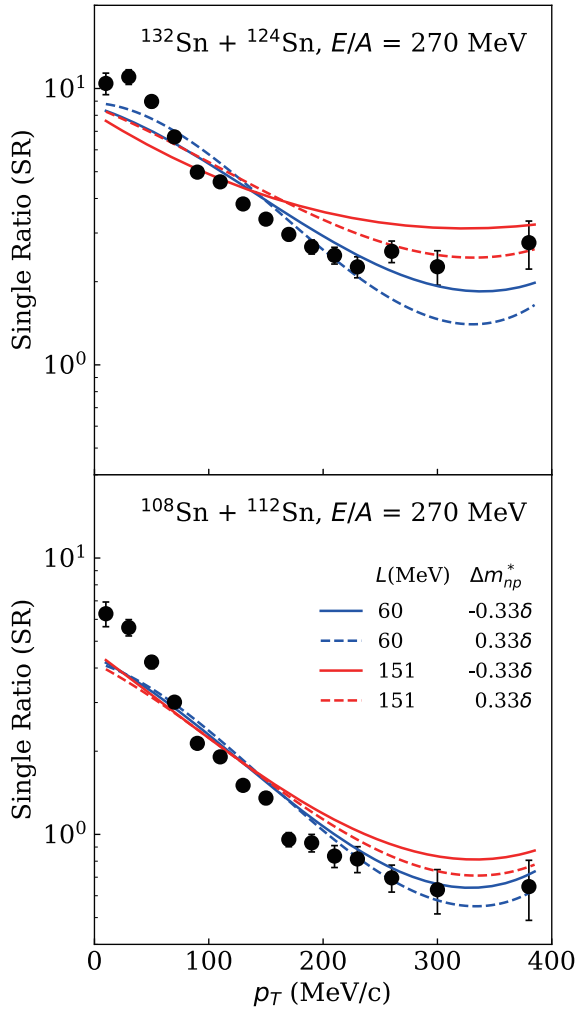

Fig. 6. Single pion spectral ratios for ^{132}Sn + ^{124}Sn (top) and ^{108}Sn + ^{124}Sn (bottom) reactions. The curves are dcQMD predictions from different L and $\Delta m*_{np}$ values. Taken from Ref. 21).

exhibit little anisotropies. With increasing impact parameter, the amount of spectator matter increases and the importance of the spectators blocking the emitted particles results in the increasing directional dependence that is characteristic of the directed flow.

Collective flow is quantified by the Fourier coefficients of the fragments' azimuthal distributions with respect to the azimuthal angle for the reaction plane Φ,[29]

$$\frac{dN}{d(\Delta\phi)} \propto 1 + 2v_1\cos(\Delta\phi) + 2v_2\cos(2(\Delta\phi)) + O, \quad (2)$$

where, N is the particle yield, $\Delta\phi$ is the azimuthal angle of emission for the particle with respective to Φ, v_1 is called the directed flow and v_2 is called the elliptic flow.

Directed flow and elliptic flow of ^{108}Sn + ^{112}Sn and ^{132}Sn + ^{124}Sn and stopping of ^{112}Sn + ^{124}Sn are extracted from the data obtained in the SπRIT

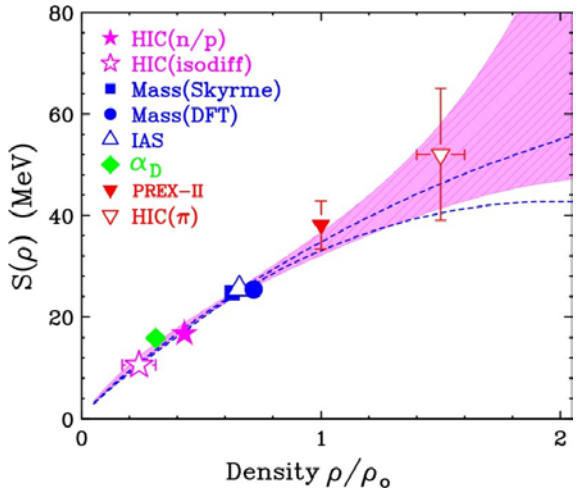

Fig. 7. Density dependence of the symmetry energy. Symbols are data given by several studies based on experiments, such as heavy-ion collision, mass, isobaric analog state and dipole polarizability. The shaded area shows the 1σ contours from empirical formula. The dashed curves represent the 1σ boundaries from fitting. Taken from Ref. 30).

experiment.[24] The measured values are compared to predictions from the Improved Quantum Molecular Dynamic-Skyrme (ImQMD-Sky) model through a Bayesian analysis, which shows strong constraining power on the effective masses and the in-medium cross-section parameter. The constraints on effective mass are converted to a probability distribution on effective mass splitting to give $\Delta m^*_{np} = -0.07^{+0.07}_{-}0.06$.

Compilation of experimental data on symmetry energy

There are several experimental studies of nuclear symmetry energy, not only with heavy-ion collision, but also with the measurement of nuclear structure properties such as neutron skin thickness and dipole polarizability. Many analyses of the nuclear EoS have been limited to extracting values for the symmetry energy, S0, and its "derivative," L, at saturation density ρ_0. This has resulted in constraints that appear contradictory. However, most experimental observables actually probe the symmetry energy at densities different from ρ_0. By focusing on the densities these observables actually probe, it is possible to obtain a detailed picture of the density dependence of the symmetry energy from 0.25 ρ_0 to 2.0 ρ_0, as shown in Fig. 7.

Bayesian analysis of combined data

Recently, a Bayesian inference study was conducted that combined data from three astrophysical multi-messenger observations of neutron stars, and twelve

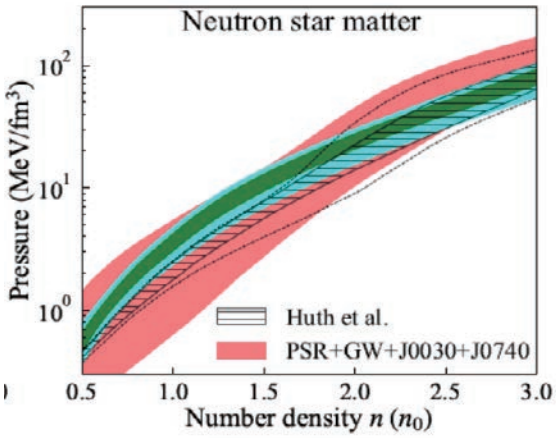

Fig. 8. Experimental (green area) and astrophysical (red area) constraints on the equation of state in pressure vs. density. The astrophysical region represents the gravitational wave and X-ray pulser PSR J0030 + 0740 constraint,[32] after converting the original unit for pressure of dyn/cm^2 to MeV/fm^3 and the for density to units of saturation density, $\rho_0 = 2.74 \times 10^14$ g/cm^3, to allow direct comparisons to nuclear physics constraints. Recent work by Huth *et al.*[33] is shown as well (HIC + χEFT + Astro). Taken from Ref. 31).

nuclear experimental constraints including SπRIT data determine the pressure of nuclear matter across a wide range of densities, as illustrated in Fig. 8.[31] This analysis shows that constraints from heavy-ion collision experiments show a remarkable consistency with multi-messenger observations and provide complementary information on nuclear matter at intermediate densities. This data-centric result provides benchmarks for theoretical calculations and modeling of nuclear matter and neutron stars. Furthermore, it provides insights into the composition of neutron stars and their cooling due to neutrino radiation.

Acknowledgments

We would like to thank members of the Transport Model Evaluation Project collaboration for many fruitful discussions. This work was supported by the U.S. National Science Foundation Grant No. PHY-2209145, the Department of Energy Grant No. DE-FG02-93ER40773, the Department of Energy National Nuclear Security Administration Stewardship Science Graduate Fellowship under cooperative Agreement No. DE-NA0002135, the Robert A. Welch Foundation (A-1266 and A-1358), the Japanese MEXT KAKENHI (Grant-in-Aid for Scientific Research on Innovative Areas) Grant No. 24105004, JSPS KAKENHI Grants Nos. JP17K05432, JP19K14709 and JP21K03528, the National Research Foundation of Korea under Grant Nos. 2018R1A5A1025563 and 2013M7A1A1075764, the Polish National Science Center (NCN) under contract Nos. UMO-2013/09/B/ST2/04064, UMO-2013/-10/M/ST2/00624, the Ministry of Science and Technology of China under Grant Nos. 2022YFE0103400 and Tsinghua University Initiative Scientific Research Program. Computing resources were provided by Facility for Rare Isotope Beams (FRIB), the HOKUSAI-Great Wave system at RIKEN under Grants Nos. G17033,Q18-23393, supported by Pioneering Program of RIKEN for Evolution of Matter in the Universe (r-EMU) and the Institute for Cyber-Enabled Research at Michigan State University.

References

1) J. M. Lattimer *et al.*, Ap. J. **550**, 426 (2001).
2) J. M. Lattimer *et al.*, Science **304**, 536 (2004).
3) P. B. Demorest *et al.*, Nature **467**, 1081 (2010).
4) J. Antoniadis *et al.*, Scie. Onli. **340**, 1233232 (2013).
5) B. P. Abbott *et al.*, Phys. Rev. Lett. **121**, 161101 (2017).
6) P. Danielewicz *et al.*, Science **298**, 1592 (2002).
7) C. Fuchs *et al.*, Prog. Part. Nucl. Phys. **56**, 1 (2006).
8) D. D. Youngblood *et al.*, Phys. Rev. Lett. **82**, 691 (1999).
9) R. Shane *et al.*, Nucl. Instrum. Methods. Phys. Res. A **784**, 513 (2015).
10) S. Tangwancharoen *et al.*, Nucl. Instrum. Methods. Phys. Res. A **853**, 44 (2017).
11) J. Barney *et al.*, Rev. Sci. Instrum. **92**, 063302 (2021).
12) E. C. Pollacco *et al.*, Nucl. Instrum. Methods. Phys. Res. A **887**, 81 (2018).
13) T. Isobe *et al.*, Nucl. Instrum. Methods. Phys. Res. A **899**, 43 (2018).
14) J. Estee *et al.*, Nucl. Instrum. Methods. Phys. Res. A **944**, 162509 (2019).
15) C. Y. Tsang *et al.*, Nucl. Instrum. Methods. Phys. Res. A **959**, 163477 (2020).
16) J. W. Lee *et al.*, Nucl. Instrum. Methods. Phys. Res. A **965**, 163840 (2020).
17) G. Jhang *et al.*, J. Korean. Phys. Soc. **69**, 144 (2016).
18) P. Lasko *et al.*, Nucl. Instrum. Methods. Phys. Res. A **856**, 92 (2017).
19) M. Kaneko *et al.*, Nucl. Instrum. Methods. Phys. Res. A **1039**, 167010 (2022).
20) G. Jhang *et al.*, Phys. Lett. B **813**, 136016 (2021).
21) J. Estee *et al.*, Phys. Rev. Lett. **126**, 162701 (2021).
22) M. Kaneko *et al.*, Phys. Lett. B **822**, 136681 (2021).
23) J. W. Lee *et al.*, Eur. Phys. J. A **58**, 201 (2022).
24) C. Y. Tsang *et al.*, Phys. Lett. B **853**, 138661 (2024).
25) V. Baran *et al.*, Phys. Rev. Lett. **86**, 4492 (2001).
26) B. A. Li *et al.*, Phys. Rev. Lett. **78**, 1644 (1997).
27) G. Stoicea *et al.*, Phys. Rev. Lett. **92**, 072303 (2004).
28) W. Reisdorf *et al.*, Nucl. Phys. A **876**, 1 (2012).
29) S. Voloshin *et al.*, Z. Phys. C, Part. Fields **70**, 665 (1996).
30) W. G. Lynch *et al.*, Phys. Lett. B **830**, 137098 (2022).
31) C. Y. Tsang *et al.*, Nat. Astro. **8**, 328 (2024).
32) I. Legred *et al.*, Phys. Rev. D **104**, 063003 (2021).
33) S. Huth *et al.*, Nature **606**, 276 (2022).